

# **1 Supplementary Information**

## **2 Self-Supervised Denoising for Enhanced Volumetric 3 Reconstruction and Signal Interpretation in 4 Two-photon Microscopy**

**5 Jie Li<sup>1,2</sup>, Liangpeng Wei<sup>3</sup>, and Xin Zhao<sup>1,2,\*</sup>**

**6** <sup>1</sup>National Key Laboratory of Intelligent Tracking and Forecasting for Infectious Diseases, Engineering Research

**7** Center of Trusted Behavior Intelligence, Ministry of Education, Tianjin Key Laboratory of Intelligent Robotic (tikLIR),

**8** Institute of Robotics & Automatic Information System (IRAIS), Nankai University, Tianjin 300350, China

**9** <sup>2</sup>Shenzhen Research Institute of Nankai University, Shenzhen 518083, China.

**10** <sup>3</sup>School of Biomedical Engineering and Technology, Tianjin Medical University, Tianjin 300070, China.

**11** \*corresponding author: Xin Zhao (zhaoxin@nankai.edu.cn)

<sup>12</sup> **CONTENTS**

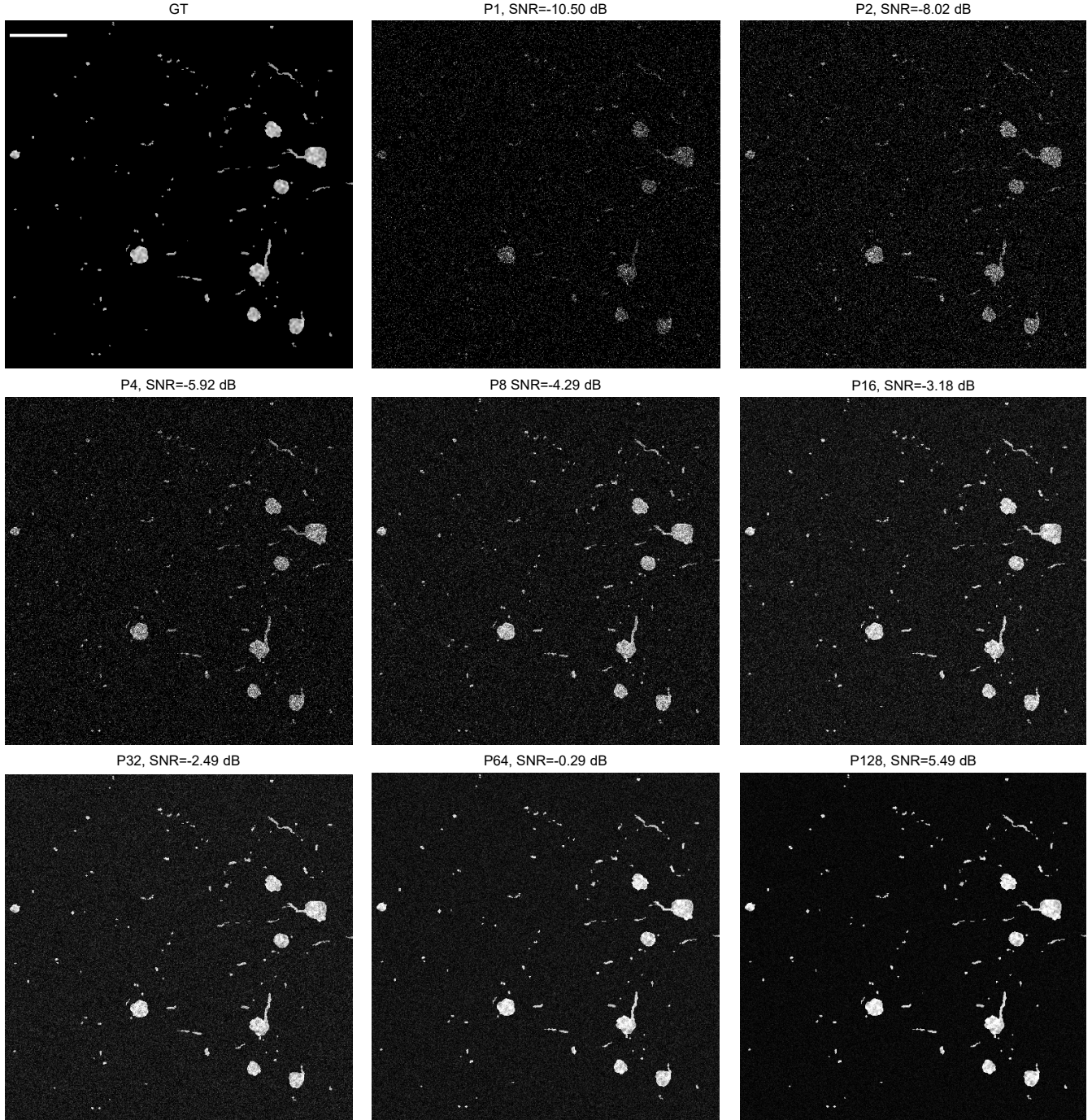
<sup>13</sup> **Supplementary Figures S1-S16**

<sup>14</sup> **Supplementary Table S1-S3**

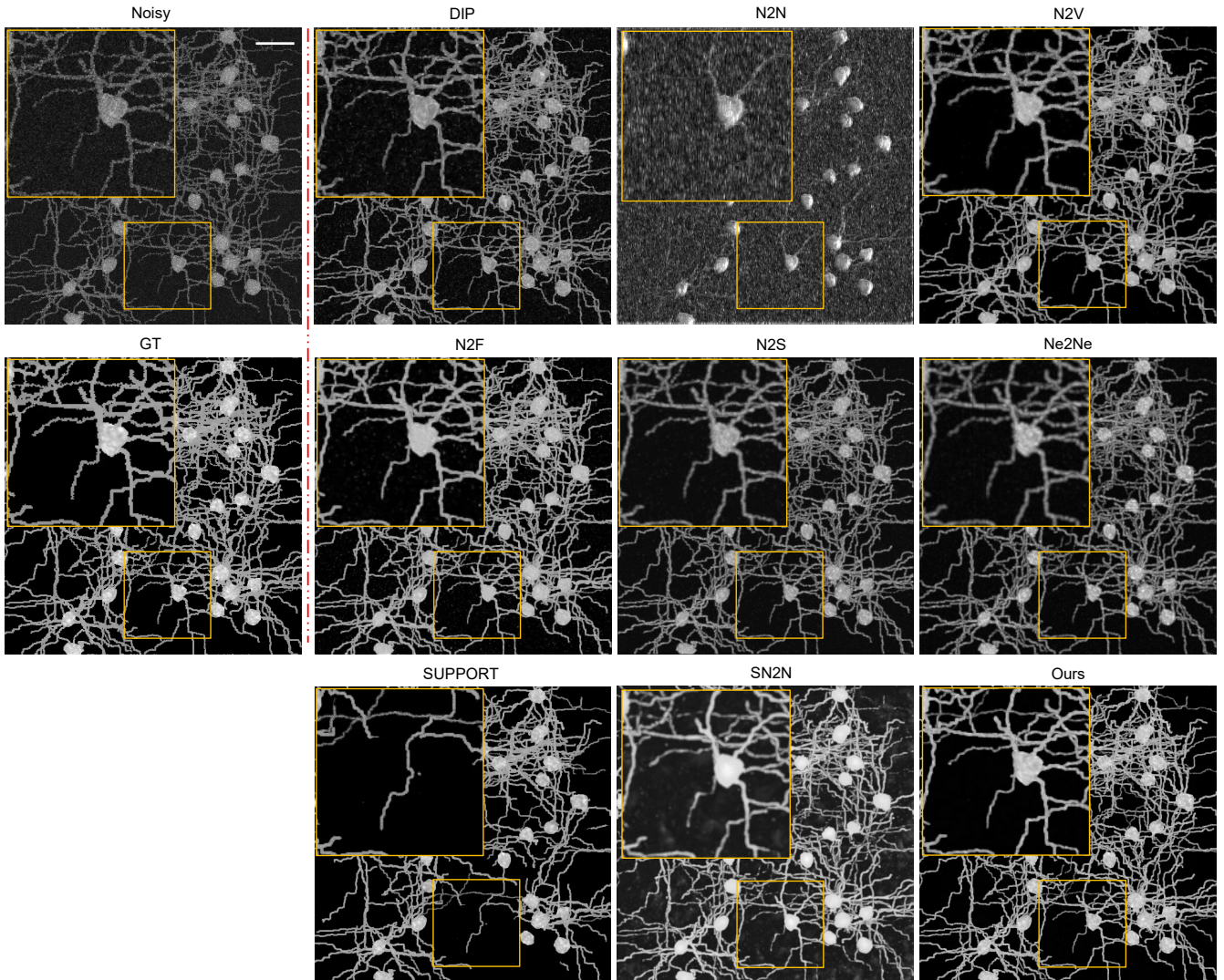
<sup>15</sup> **Supplementary Notes S1**

<sup>16</sup> **Supplementary Videos S1-S9**

17 **Supplementary Figures**

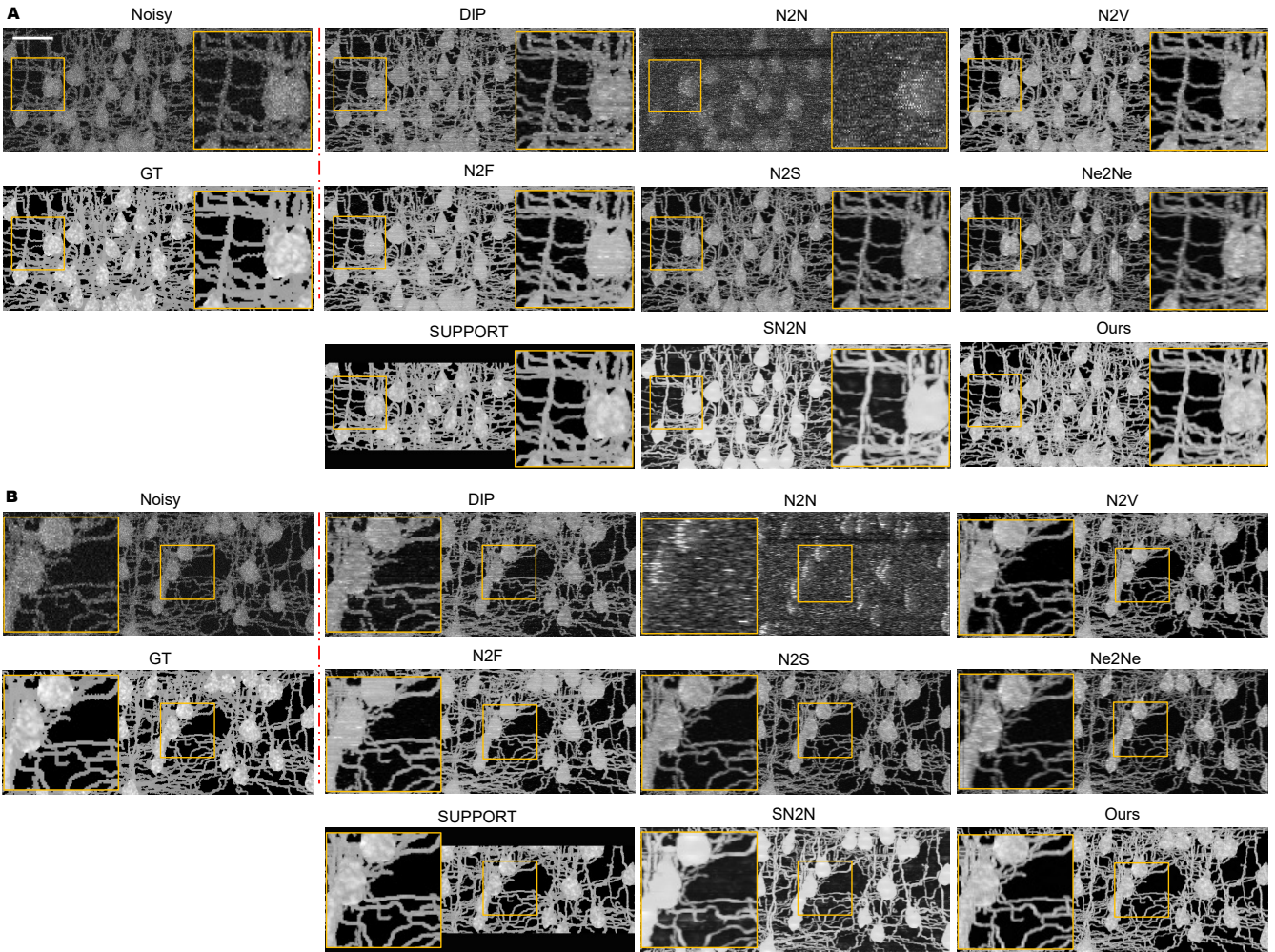


**Supplementary Fig. S1. Simulation of structural imaging data.** Representative images of different imaging SNRs and corresponding ground truth (GT). Noise-free structural imaging stacks were simulated based on NAOMi<sup>1</sup>. Different levels of Mixed Poisson-Gaussian noise were added subsequently. Noise-free images were used as the ground truth for quantitative evaluations of the denoising performance. Scale bar, 50  $\mu m$ .



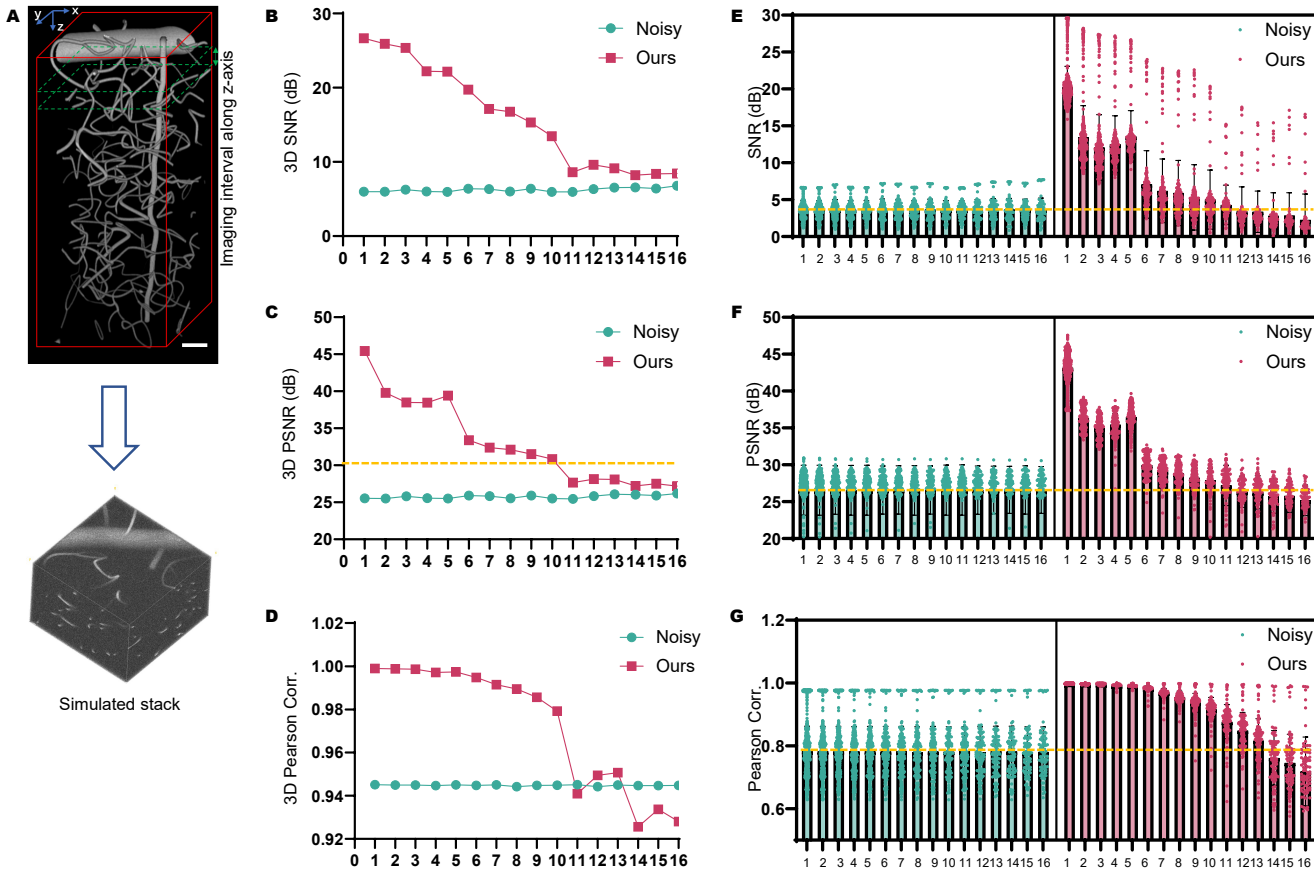
19

**Supplementary Fig. S2. Max projection images for method comparison.** Max projection images along the z-axis of the whole volume with  $250 \times 250 \times 100 \mu m^3$  (200 planes,  $0.5 \mu m/pixel$  in three axes), for comparison of different methods.



20

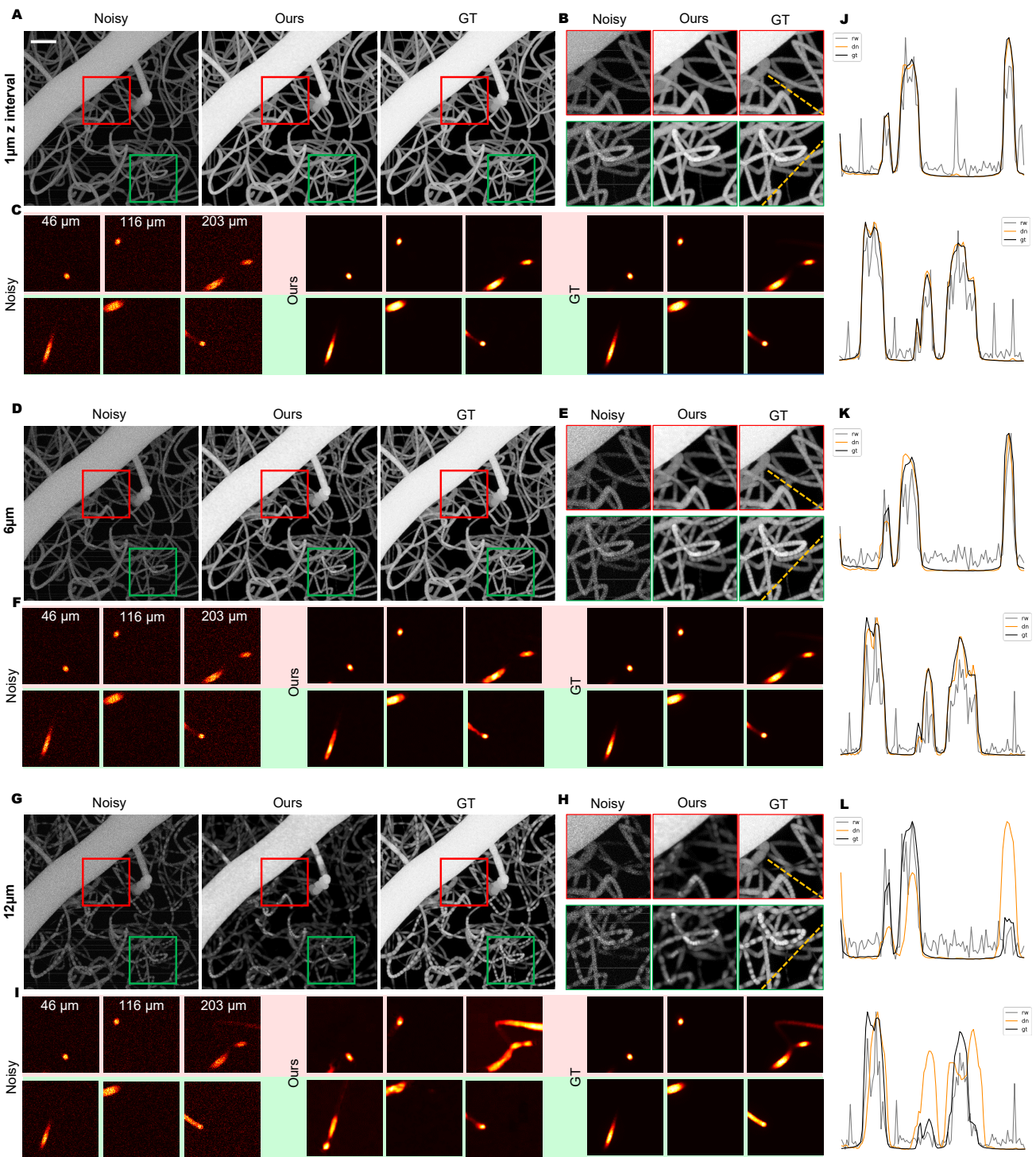
**Supplementary Fig. S3. Max projection images for method comparison.** **A**, Max projection images along y axis of the whole volume with  $250 \times 250 \times 100 \mu\text{m}^3$  (200 planes,  $0.5 \mu\text{m}/\text{pixel}$  in three axes), for comparison of different methods. Scale bar,  $50 \mu\text{m}$ . Magnified views of yellow-boxed regions are shown at the right of each image. **B**, Max projection images along x axis of the whole volume with  $250 \times 250 \times 100 \mu\text{m}^3$  (200 planes,  $0.5 \mu\text{m}/\text{pixel}$  in three axes), for comparison of different methods. Scale bar,  $50 \mu\text{m}$ . Magnified views of yellow-boxed regions are shown at the left of each image.



21

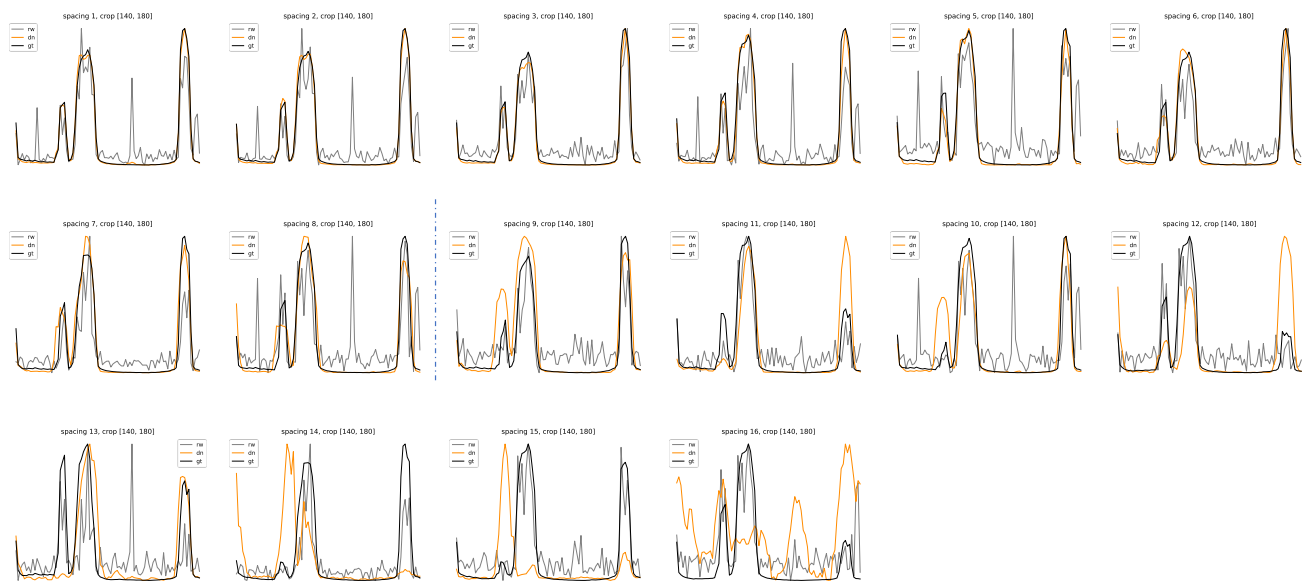
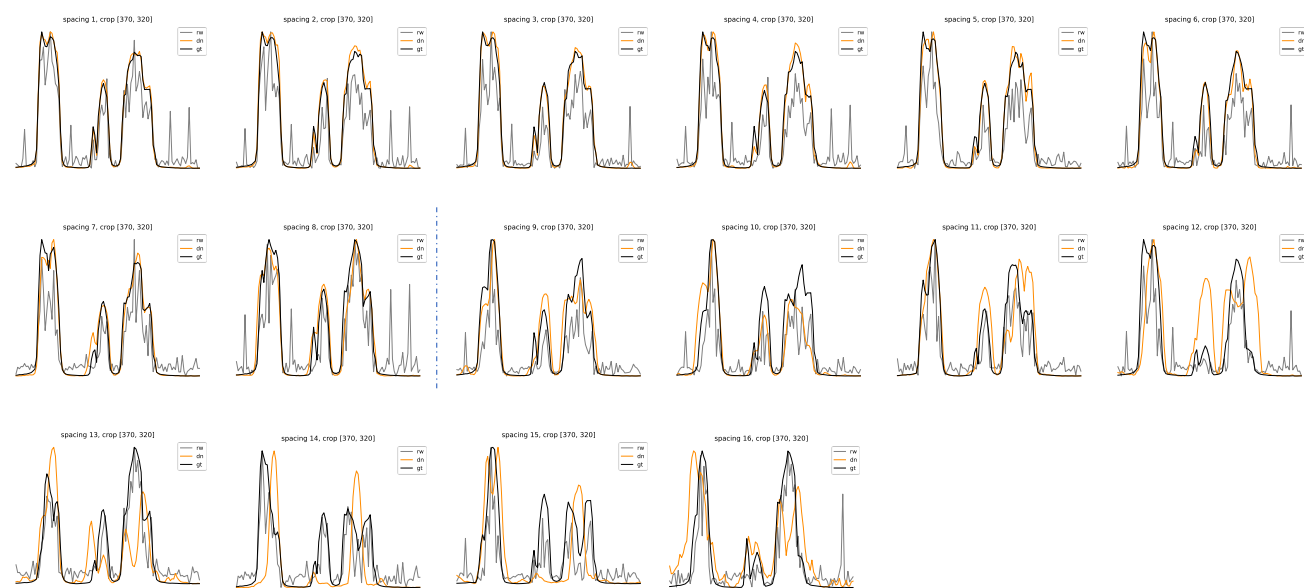
### Supplementary Fig. S4. Quantitative results with different imaging intervals along the z-axis. A,

A spatial vasculature was first constructed, comprising three parts: surface vessels ( $4\text{--}30 \mu\text{m}$  in diameter), primarily distributed laterally in superficial layers; diving vessels ( $9\text{--}11 \mu\text{m}$ ), located deeper in the tissue; and capillaries ( $2 \mu\text{m}$ ), distributing throughout the volumetric space. Then the imaging intervals along the z-axis were adjusted to obtain 16 different simulated two-photon image stacks by NAOMi<sup>1</sup>, ranging from  $1 \mu\text{m}$  to  $16 \mu\text{m}$ . Scale bar,  $25 \mu\text{m}$ . **B**, 3D SNR **C**, 3D PSNR and **D**, 3D Pearson correlation from 16 different image stacks. The yellow dashed link in B indicates the high-quality image baseline. **E**, SNR **F**, PSNR and **G**, Pearson correlation statistical results along xy plane from 16 different image stacks. The yellow dashed link in E F G indicates the baseline of the noisy sequence.

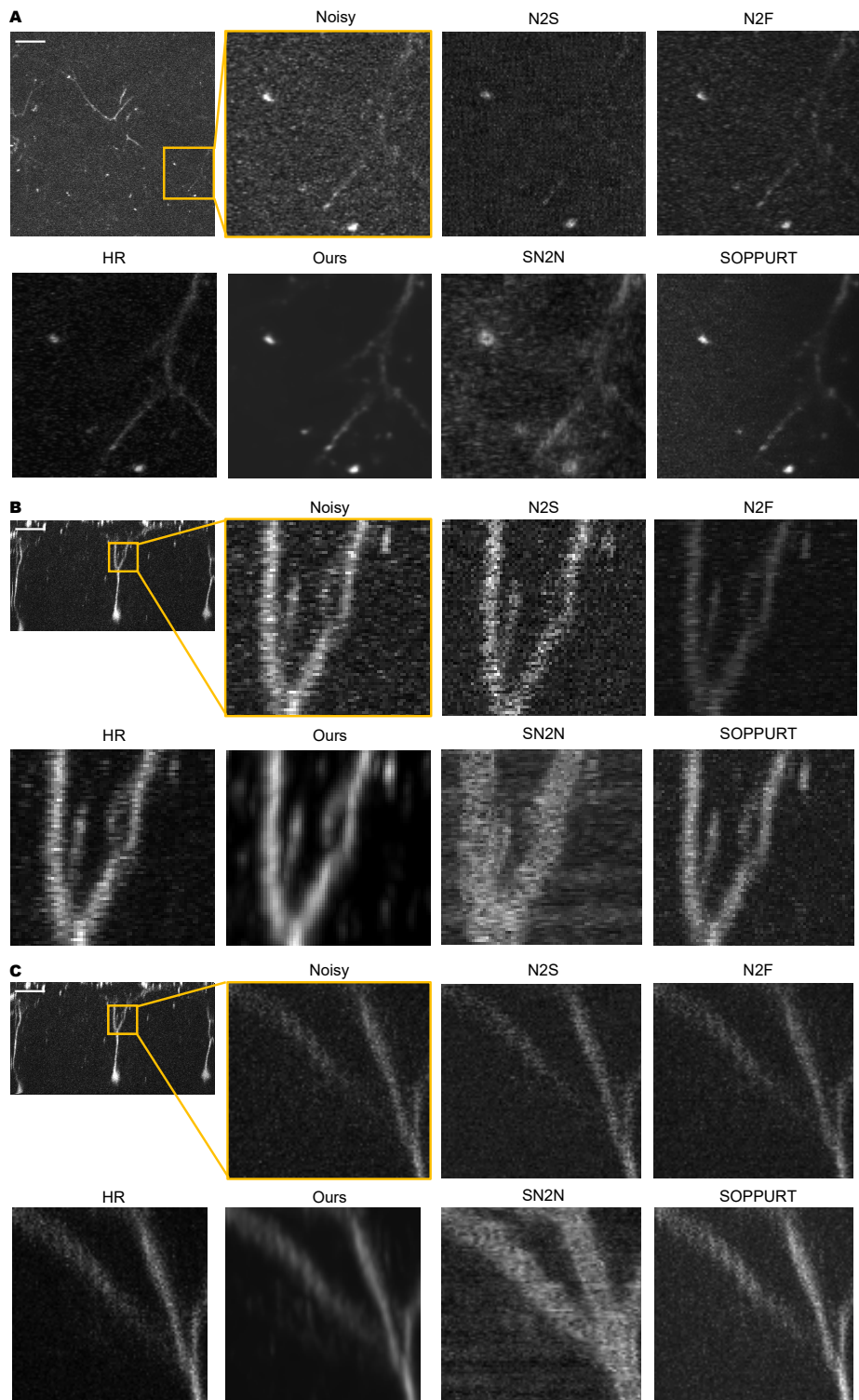


**Supplementary Fig. S5. Qualitative results with different imaging intervals along the z-axis.**

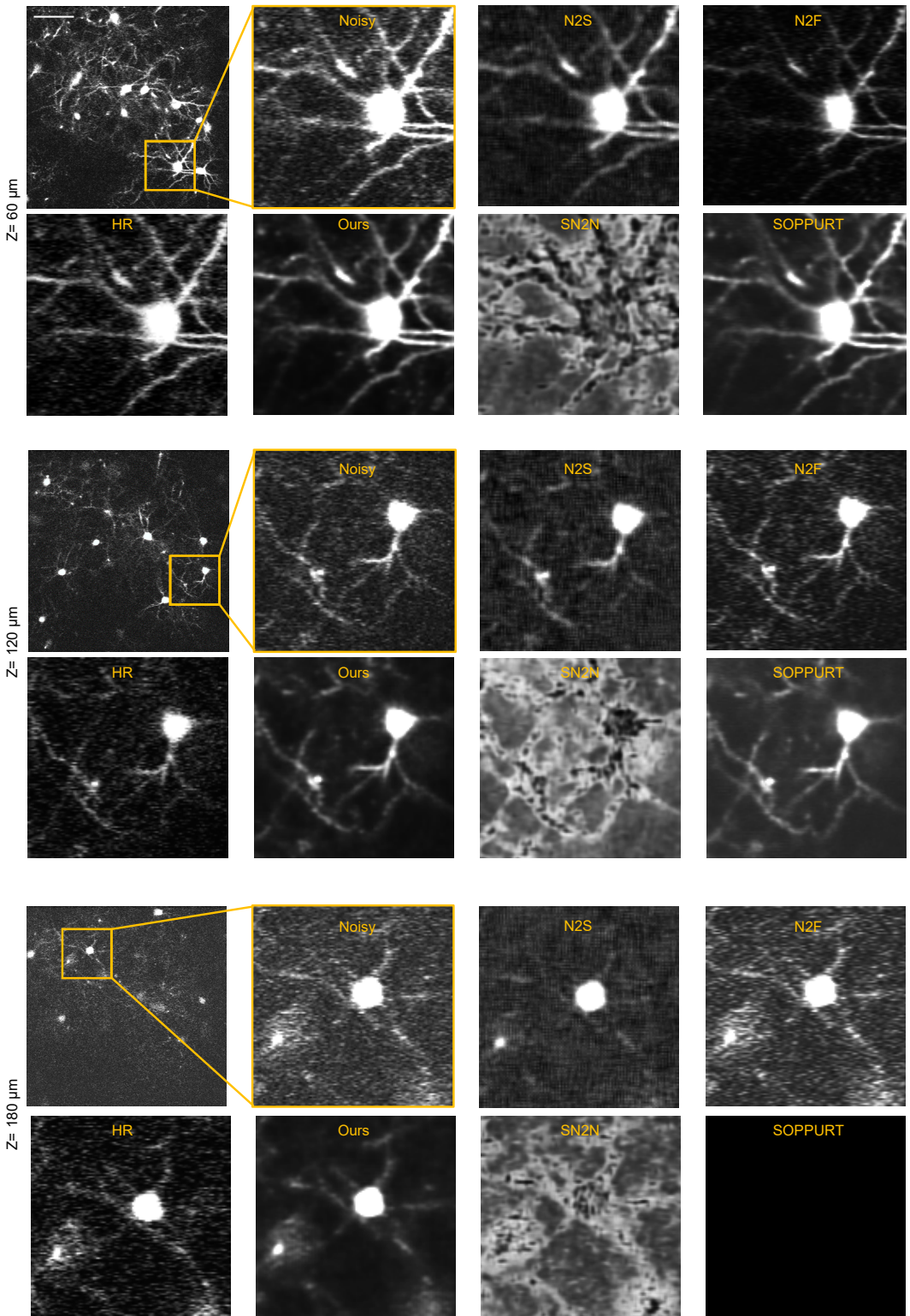
**A**, Max projection along the z-axis before and after denoising by SelfMirror, from the  $1 \mu m$  imaging interval. Scale bar,  $30 \mu m$ . **B**, Magnified views of the red and green box regions in A, respectively. **C**, Representative images of three different depths in the red and green regions in A. **D**, Max projection along the z-axis before and after denoising, from the  $6 \mu m$  imaging interval. **E**, Magnified views of the red and green box regions in D, respectively. **F**, Representative images of three different depths in the red and green regions in D. **G**, Max projection along the z-axis before and after denoising, from the  $12 \mu m$  imaging interval. **H**, Magnified views of the red and green box regions in G, respectively. **I**, Representative images of three different depths in the red and green regions in G. **J**, **K**, and **L** are pixel intensity traces of the dashed lines (in the red and green regions) in B, E, and H, respectively.

**A****B**

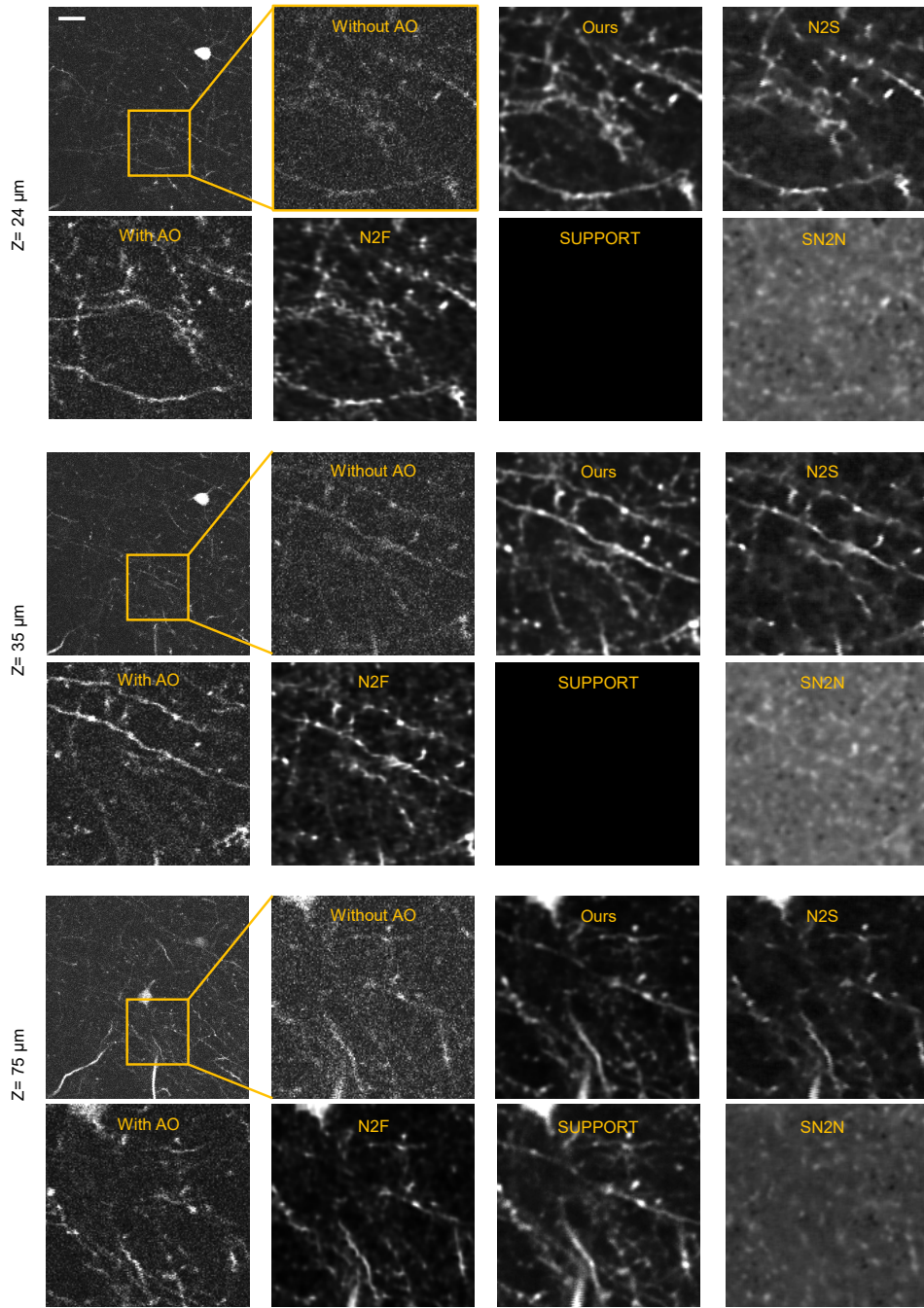
**Supplementary Fig. S6. pixel trace results from the 16 z intervals.** **A**, Pixel intensity traces extracted from the dashed line as in the red region in Fig. **S5B**, from 16 imaging intervals, respectively. **B**, Pixel intensity traces extracted from the dashed line as in the green region in Fig. **S5B**, from 16 imaging intervals, respectively. The vertical dashed blue lines in A and B demonstrate the critical imaging interval threshold of  $8 \mu m$ . The imaging interval of less than  $8 \mu m$  demonstrates superior denoising efficacy with close alignment to GT, whereas the imaging interval of more than  $8 \mu m$  shows progressive drift.



**Supplementary Fig. S7. Denoising experimentally single neuron data with synchronized high-SNR reference.** **A**, Representative max projections along the z-axis before and after denoising, which were used for pixel traces in Fig. 3D. 20 xy slices for this projection. Scale bar, 50  $\mu m$ . Magnified views of yellow-boxed regions are shown. **B**, Representative max projections along the y-axis before and after denoising, which were used for the pixel traces in Fig. 3E. 200 xz slices for this projection. Scale bar, 50  $\mu m$ . Magnified views of yellow-boxed regions are shown. **C**, Representative max projections along the x-axis before and after denoising, which were used for the pixel traces in Fig. 3E. 100 xy slices for this projection. Scale bar, 50  $\mu m$ . Magnified views of yellow-boxed regions are shown.

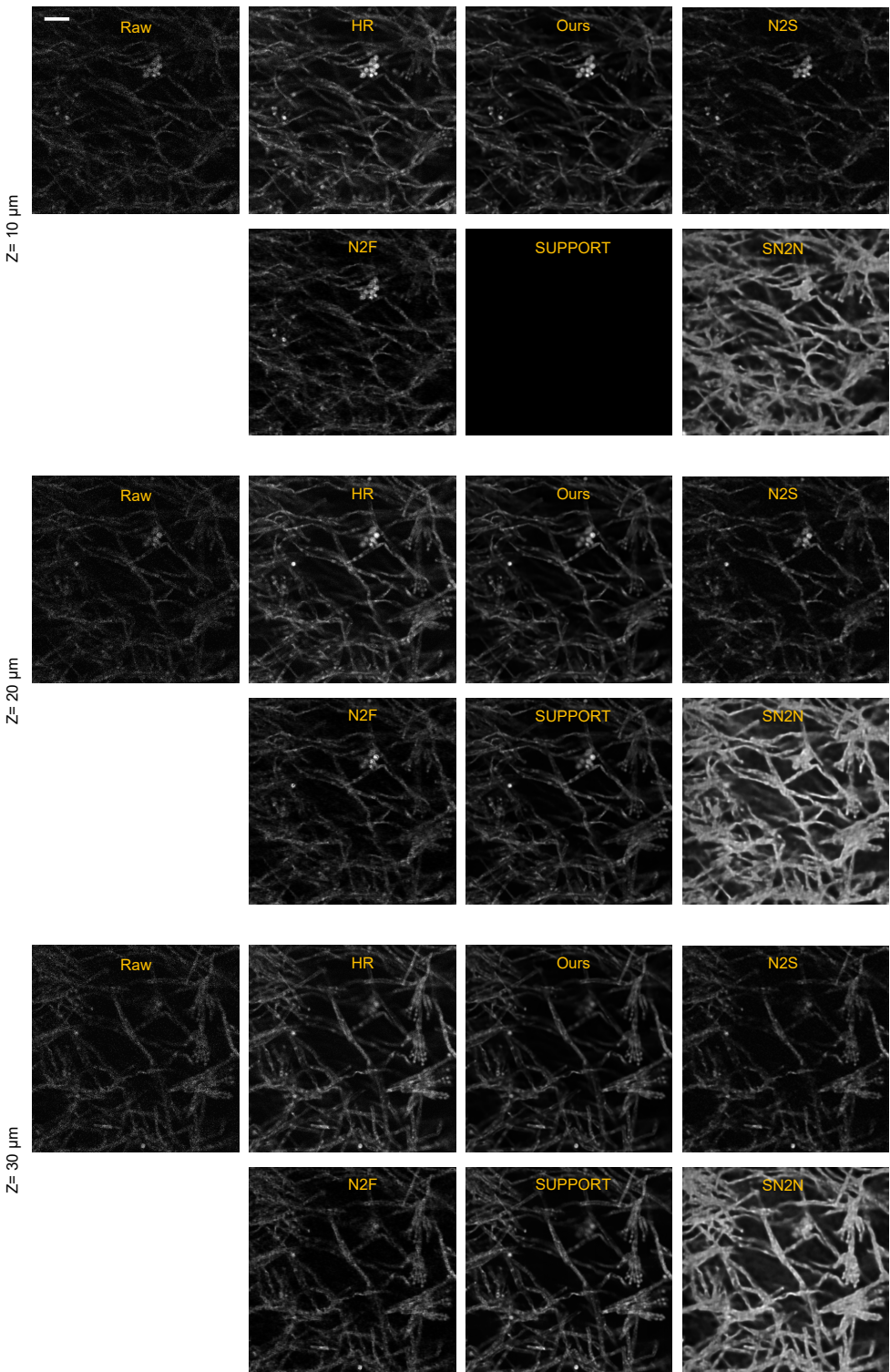


**Supplementary Fig. S8. Denoising experimentally neuronal population data with synchronized high-SNR reference.** Two-photon volumetric imaging neuronal population data were used to train our method, and high-SNR data were used as a reference. Three slices at different depths are represented here. Scale bar,  $50 \mu m$ . Magnified views of yellow-boxed regions are shown.



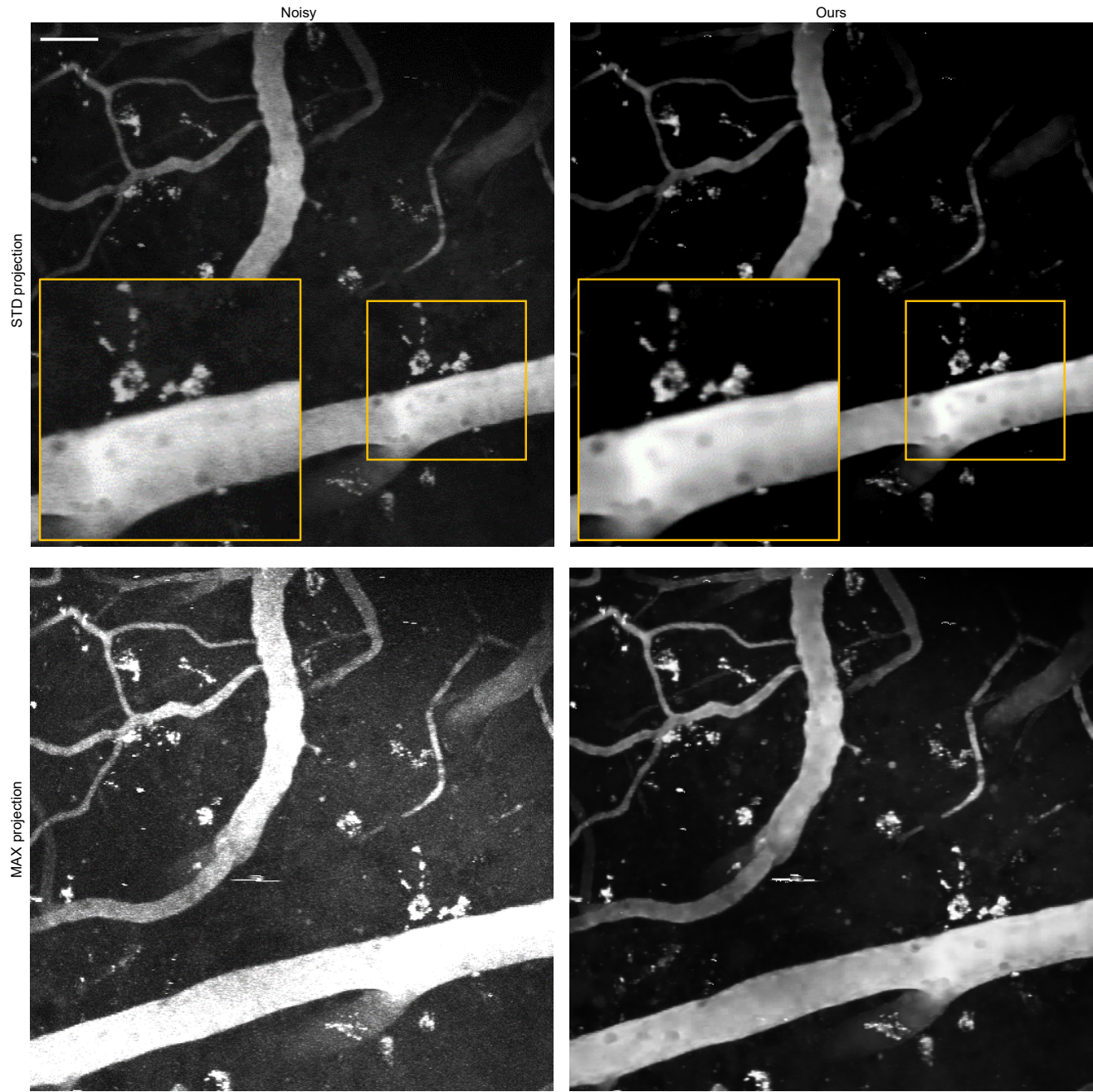
26

**Supplementary Fig. S9. Denoising structural imaging data of dendrite and spine with synchronized high-SNR reference.** Two-photon without AO imaging data of dendrite and spine were used to train our method, with AO data used as a reference. Three slices at different depths are represented here and each row shows one slice. Scale bar, 25  $\mu m$ .



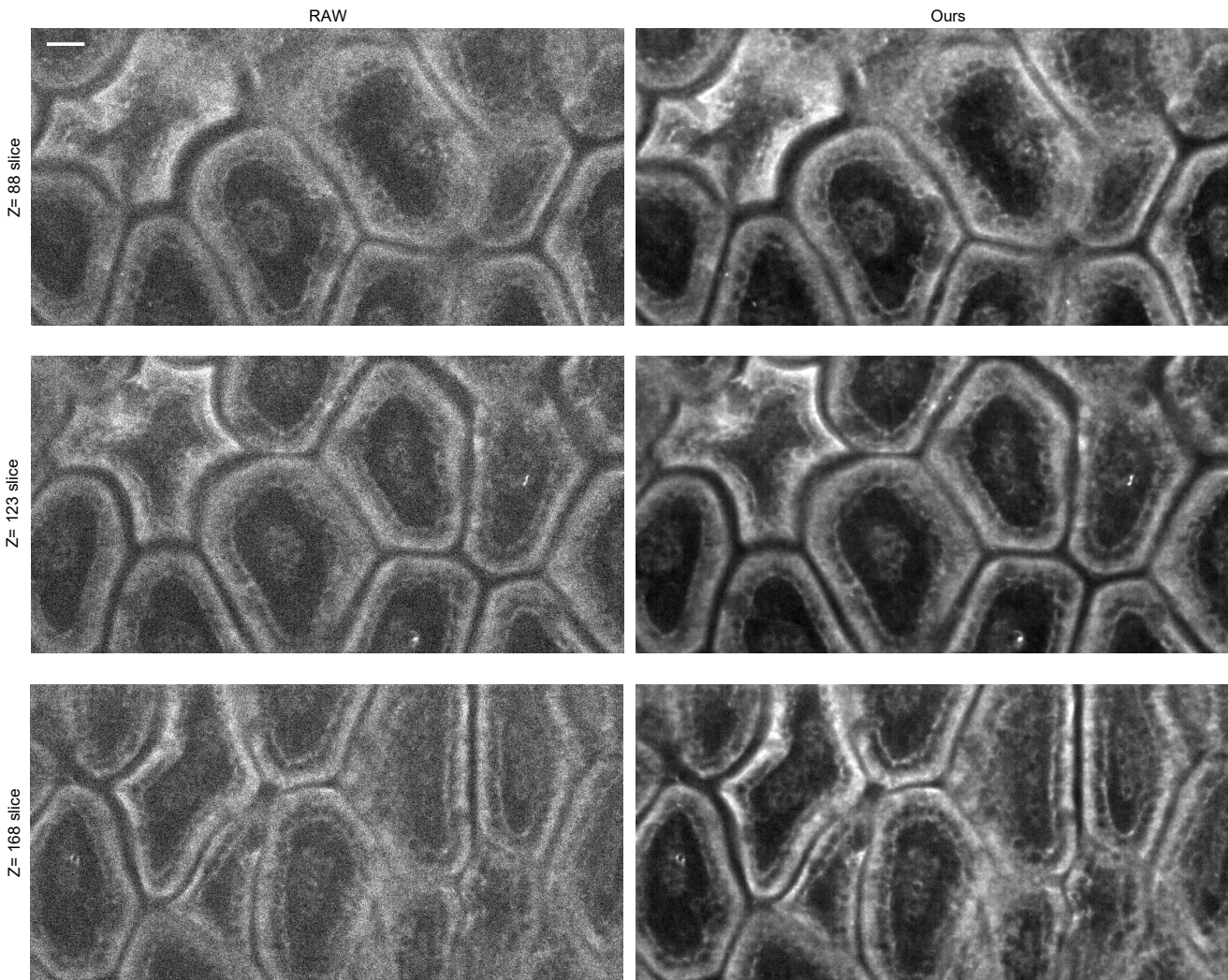
**Supplementary Fig. S10. Applying SelfMirror on volumetric structural imaging of Penicillium.**

Volumetric structural imaging of Penicillium was used to train our method, and high-SNR data were used as a reference. Three slices at different depths are represented here. Scale bar, 5  $\mu m$ . Magnified views of yellow-boxed regions are shown.



28

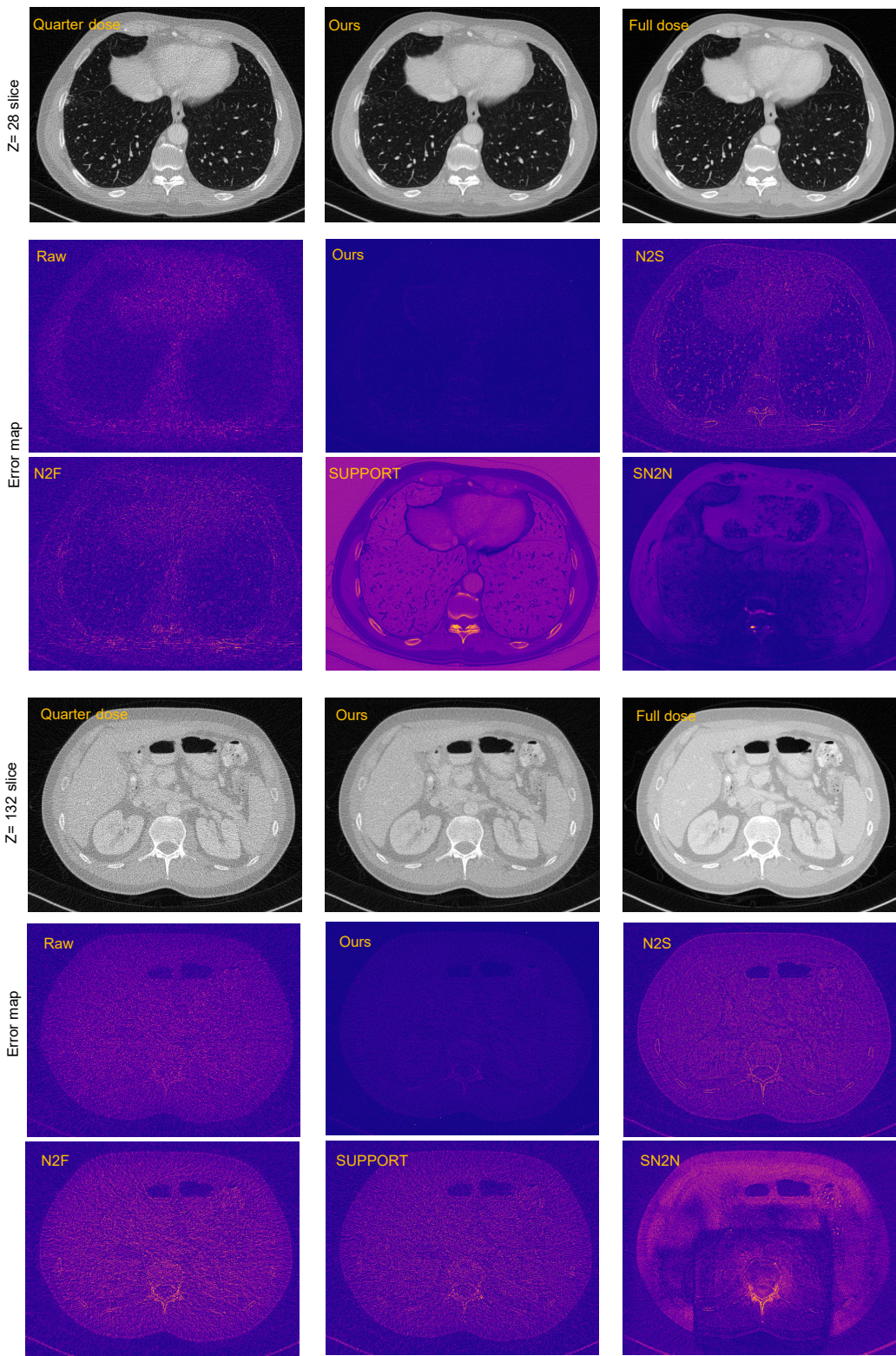
**Supplementary Fig. S11. Applying SelfMirror on two-photon imaging of vessel sample.** STD projection (top) and Max projection (bottom) of vessel data of a mouse cortex with a  $250 \times 250 \times 100 \mu\text{m}^3$  volume. Left, raw data. Right, corresponding images using SelfMirror. Scale bars,  $30 \mu\text{m}$ . Magnified views of yellow-boxed regions are shown at the left bottom of each image.



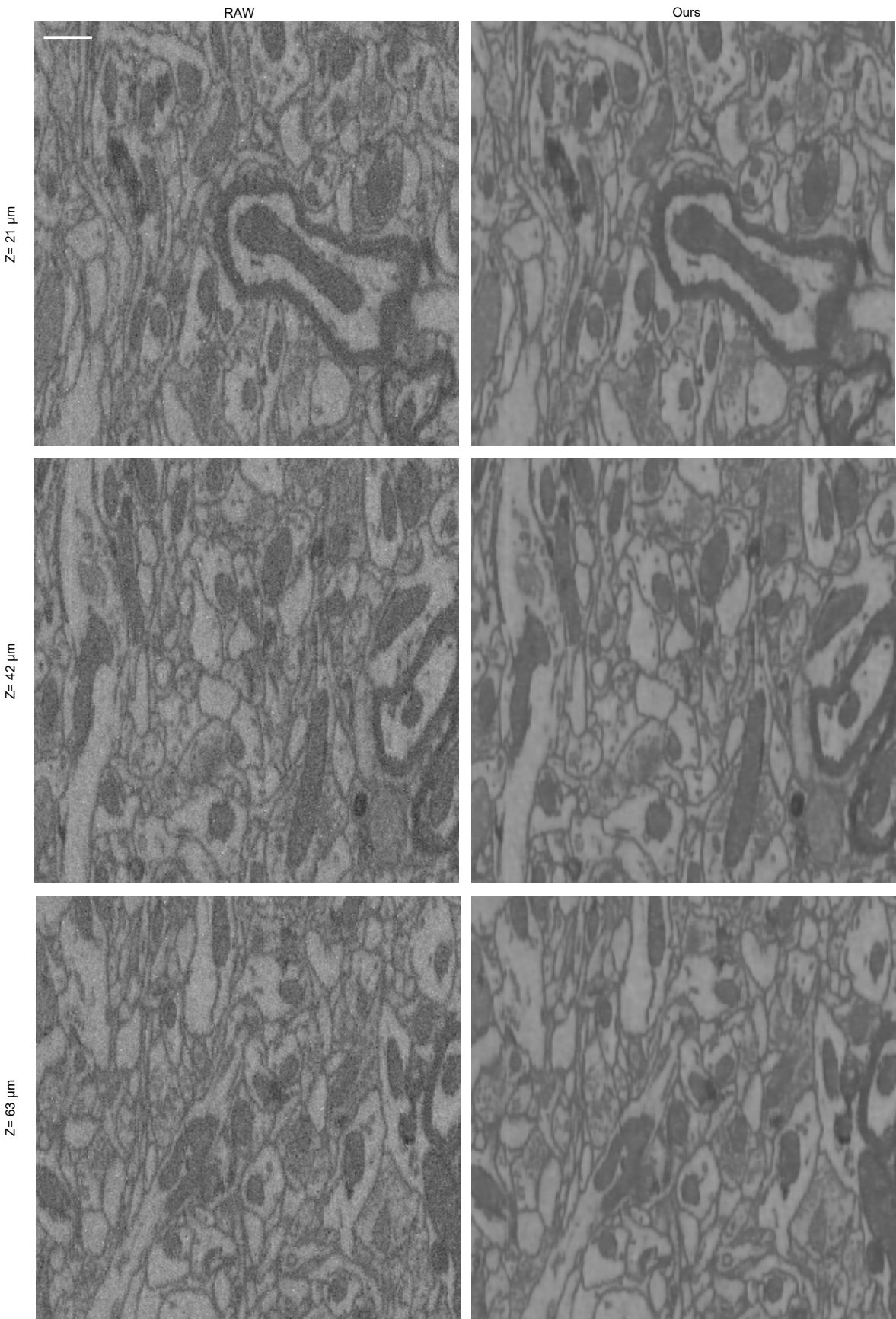
29

**Supplementary Fig. S12. Applying SelfMirror on the intestine of a mouse embryo after expansion.**

Light sheet microscopy imaging data of the intestine of a mouse embryo after expansion. Three slices at different depths are represented here and each row shows one slice. Scale bar,  $30 \mu m$ .



**Supplementary Fig. S13. Applying SelfMirror on CT of a male's pleuroperitoneal cavity.** CT data of the intestine of a male's pleuroperitoneal cavity. Two slices at different depths are represented here and each row shows one slice and the corresponding error map below the slice. Full-dose CT data were used as the high-SNR reference. Left, quarter dose low-SNR images. Middle, SelfMirror denoising images. Right, full dose high-SNR images. Error maps are given to show the pixel variance among different denoising methods.

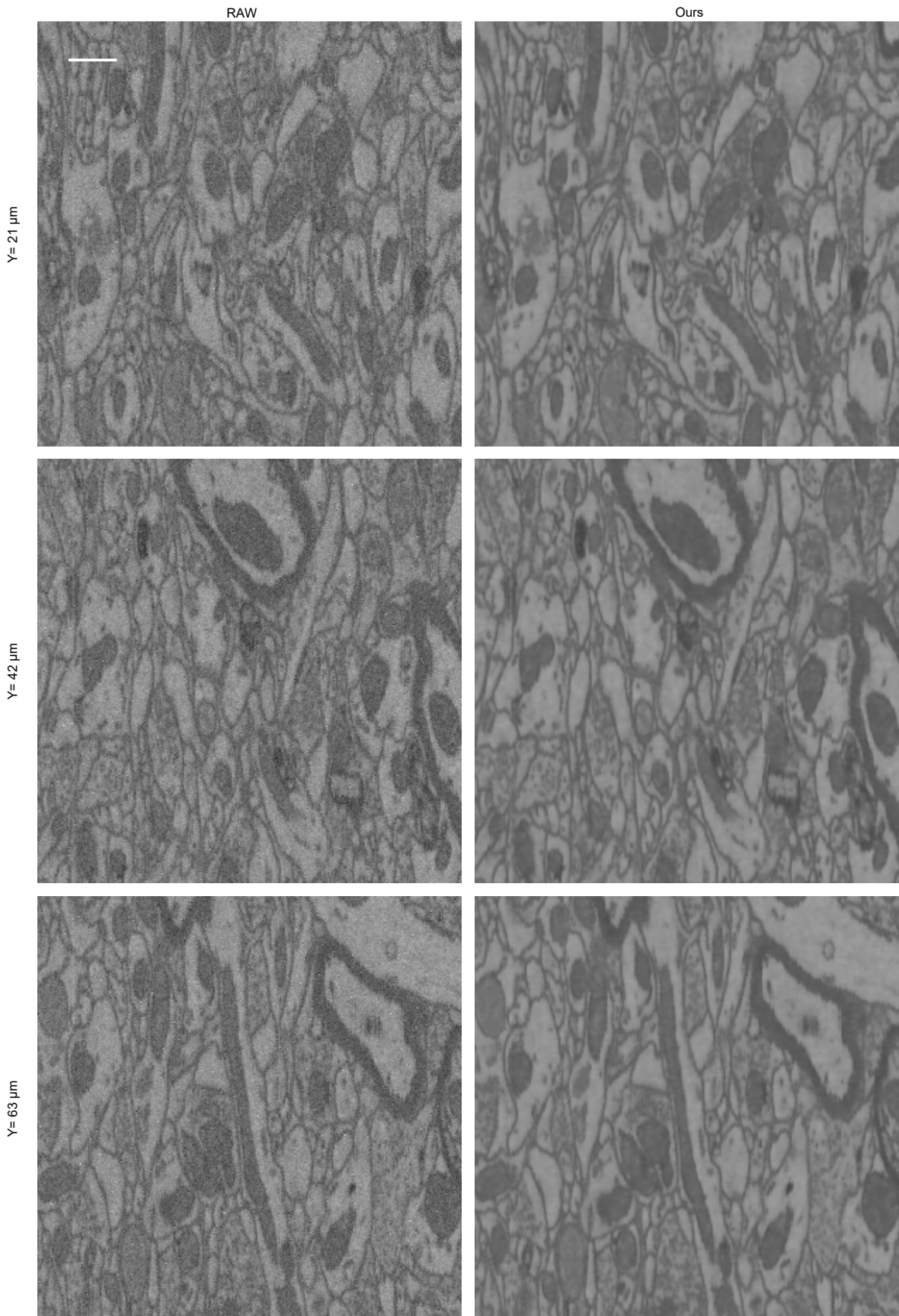


**Supplementary Fig. S14. Applying SelfMirror on SEM data of a mouse somatosensory cortex**

**layer 4 .** SEM data of a mouse somatosensory cortex layer 4 with a  $93 \times 60 \times 93 \mu\text{m}^3$ . Left, raw data.

Right, corresponding images using SelfMirror. Three slices at different z depths are represented here.

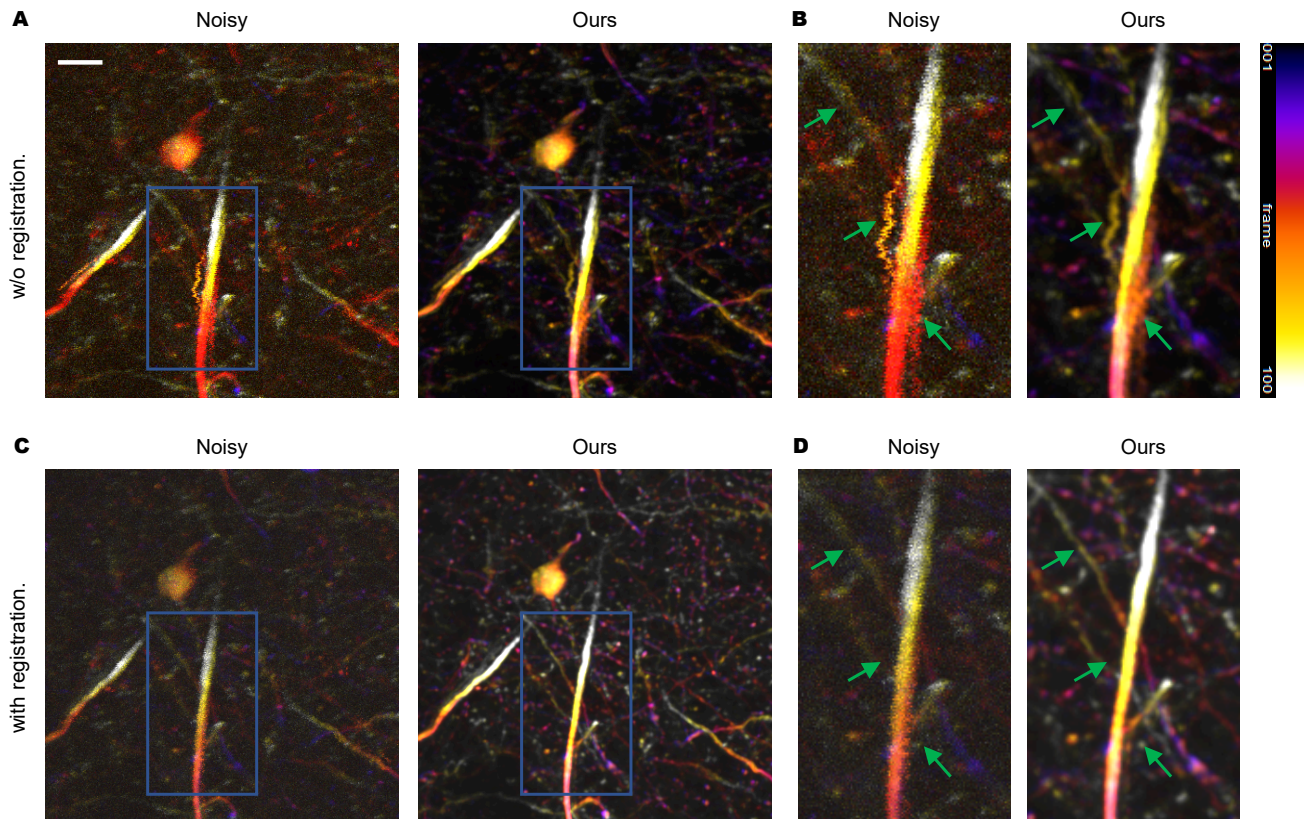
Scale bar, 10  $\mu\text{m}$ .



**Supplementary Fig. S15. Applying SelfMirror on SEM data of a mouse somatosensory cortex**

**layer 4 .** SEM data of a mouse somatosensory cortex layer 4 with a  $93 \times 60 \times 93 \mu\text{m}^3$ . Left, raw data.

Right, corresponding images using SelfMirror. Three slices at different depths along y axis are represented here and each row shows one slice. Scale bar,  $10 \mu\text{m}$ .



33

**Supplementary Fig. S16. Denoising two-photon dendrite image stack before and after drift registration. A, Z-color projection of noisy (left) and denoised (right) images, without registration. Scale bar, 25  $\mu\text{m}$ . B, Magnified views of the blue rectangle regions in A. Green arrows indicate that the drift happens during imaging on the left, and the over-smooth artifact and pseudomorph after denoising on the right. C, Z-color projection of noisy (left) and denoised (right) images, with registration. B, Magnified views of the blue rectangle regions in C. Green arrows corresponding to the arrows in B. The drift in the left image is largely suppressed after registration, and after denoising, over-smoothing and artifacts are significantly reduced.**

<sup>34</sup> **Supplementary Tables**

<sup>35</sup> **Supplementary Table S1:** Comparison of PSNR (upper table) and Pearson correlation coefficient (bottom  
<sup>36</sup> table) along the z axis of the whole volume.

<sup>37</sup> **Supplementary Table S2:** Comparison of PSNR (upper table) and Pearson correlation coefficient (bottom  
<sup>38</sup> table) along the y axis of the whole volume.

<sup>39</sup> **Supplementary Table S3:** Comparison of PSNR (upper table) and Pearson correlation coefficient (bottom  
<sup>40</sup> table) along the x axis of the whole volume.

<sup>41</sup>

<sup>42</sup> **Supplementary Note**

<sup>43</sup> **S1. Proof of SelfMirror**

<sup>44</sup> Theoretically, the low-SNR image  $X$  can be decomposed into the sample signals  $G$ , representing ground  
<sup>45</sup> truth, and noise  $N$ , in our case, the zero-mean Poisson–Gaussian additive noise. Thus, the low-SNR  
<sup>46</sup> images can be represented as:

$$X = G + N \quad (1)$$

<sup>47</sup> It's probabilistic form:  $p(X) = p(G)p(N|G)$ . Normally, we assume that noise of each pixel is independent,  
<sup>48</sup> while the signal is not. That is  $\forall i \neq j, p(N(i)) = p(N(i)|N(j))$ , while  $\forall (i, j), p(G(i)) \neq p(G(i)|G(j)), i, j$   
<sup>49</sup> are the pixel indexes of a volume image. Consider  $X_1$  and  $X_2$  are two sub-volumes using SelfMirror's strate-  
<sup>50</sup> gies from a single volume image  $X$ . Assume that  $X_1$  and  $X_2$  are two independent noisy images conditioned  
<sup>51</sup> on noise-free volume  $G^{2,3}$ . Suppose that there exists a  $\varepsilon \neq 0$ , so that  $\mathbb{E}_{X_1|G}(X_1) = G, \mathbb{E}_{X_2|G}(X_2) = G + \varepsilon$ ,  
<sup>52</sup>  $\mathbb{E}_{X_1, X_2|G}(X_1 - X_2) = \varepsilon$ , and  $\sigma_2^2$  is the variance of  $X_2$ . We have:

$$\begin{aligned} \mathbb{E}_{X_1|G} \|f_\theta(X_1) - G\|_2^2 &= \mathbb{E}_{X_1, X_2|G} \|f_\theta(X_1) - X_2 + X_2 - G\|_2^2 \\ &= \mathbb{E}_{X_1, X_2|G} \|f_\theta(X_1) - X_2\|_2^2 + \mathbb{E}_{X_2|G} \|X_2 - G\|_2^2 \\ &\quad + 2\mathbb{E}_{X_1, X_2|G}(f_\theta(X_1) - X_2)^\top (X_2 - G) \\ &= \mathbb{E}_{X_1, X_2|G} \|f_\theta(X_1) - X_2\|_2^2 + \sigma_2^2 \\ &\quad + 2\mathbb{E}_{X_1, X_2|G}(f_\theta(X_1) - G + G - X_2)^\top (X_2 - G) \quad (2) \\ &= \mathbb{E}_{X_1, X_2|G} \|f_\theta(X_1) - X_2\|_2^2 + \sigma_2^2 + 2\mathbb{E}_{X_1, X_2|G}(f_\theta(X_1) - G)^\top (X_2 - G) \\ &\quad + 2\mathbb{E}_{X_2|G}(G - X_2)^\top (X_2 - G) \\ &= \mathbb{E}_{X_1, X_2|G} \|f_\theta(X_1) - X_2\|_2^2 - \sigma_2^2 + 2\mathbb{E}_{X_1, X_2|G}(f_\theta(X_1) - G)^\top (X_2 - G) \end{aligned}$$

- 53 Due to the independence between  $X_1$  and  $X_2$  given  $G$ , we transform the last term  $\mathbb{E}_{X_1, X_2 | G}(f_\theta(X_1) - G)^\top (X_2 - G)$  in Equation 2:

$$\begin{aligned}
 \mathbb{E}_{X_1, X_2 | G}(f_\theta(X_1) - G)^\top (X_2 - G) &= \mathbb{E}_{X_1, X_2 | G}(f_\theta(X_1) - G)^\top (X_2 - X_1 + X_1 - G) \\
 &= \mathbb{E}_{X_1, X_2 | G}(f_\theta(X_1) - G)^\top (X_2 - X_1) \\
 &\quad + \mathbb{E}_{X_1, X_2 | G}(f_\theta(X_1) - G)^\top (X_1 - G) \\
 &= \varepsilon \mathbb{E}_{X_1 | G}(f_\theta(X_1) - G)
 \end{aligned} \tag{3}$$

- 55 Combine Equation 2 and Equation 3, we have:

$$\mathbb{E}_{X_1 | G} \|f_\theta(X_1) - G\|_2^2 = \mathbb{E}_{X_1, X_2 | G} \|f_\theta(X_1) - X_2\|_2^2 - \sigma_2^2 + 2\varepsilon \mathbb{E}_{X_1 | G}(f_\theta(X_1) - G) \tag{4}$$

- 56 Since both  $X_1$  and  $X_2$  are conditioned on  $G$ , we finally have:

$$\mathbb{E}_{G, X_1} \|f_\theta(X_1) - G\|_2^2 = \mathbb{E}_{G, X_1, X_2} \|f_\theta(X_1) - X_2\|_2^2 - \sigma_2^2 + 2\varepsilon \mathbb{E}_{G, X_1}(f_\theta(X_1) - G) \tag{5}$$

- 57 If  $\mathbb{E}_{X_1, X_2 | G}(X_1 - X_2) = \varepsilon$  is near 0, that is  $X_1$  and  $X_2$  are closely similar, then we can train the network with  
 58 noisy sub-stack  $(X_1, X_2)$ , and obtain trained output as a reasonable approximation to ground-truth  $G$ .

59 **Supplementary Videos**

60 **Supplementary Video S1 (Visualization 1).** Simulated volumetric structural imaging of  
61 neurons.

62 **Supplementary Video S2 (Visualization 2).** Two-photon volumetric imaging of single  
63 neurons in mouse cortex.

64 **Supplementary Video S3 (Visualization 3).** Two-photon volumetric imaging of neuronal  
65 population in mouse cortex.

66 **Supplementary Video S4 (Visualization 4).** Two-photon volumetric imaging of neuronal  
67 dendrites of mouse.

68 **Supplementary Video S5 (Visualization 5).** Confocal microscopy volumetric structural  
69 imaging of penicillin.

70 **Supplementary Video S6 (Visualization 6).** Two-photon volumetric imaging of cerebrovas-  
71 culature of mouse.

72 **Supplementary Video S7 (Visualization 7).** Expansion microscopy volumetric structural  
73 imaging of the intestine of mouse embryos.

74 **Supplementary Video S8 (Visualization 8).** Computed tomography of human thoracoab-  
75 dominal body.

76 **Supplementary Video S9 (Visualization 9).** Scanning electron microscopy volumetric  
77 imaging of cells from mouse cortex.

<sup>78</sup> **References**

- <sup>79</sup> **1.** Song, A., Gauthier, J. L., Pillow, J. W., Tank, D. W. & Charles, A. S. Neural anatomy and optical  
<sup>80</sup> microscopy (naomi) simulation for evaluating calcium imaging methods. *J. neuroscience methods* **358**,  
<sup>81</sup> 109173 (2021).
- <sup>82</sup> **2.** Lequyer, J., Philip, R., Sharma, A., Hsu, W.-H. & Pelletier, L. A fast blind zero-shot denoiser. *Nat.  
83 Mach. Intell.* **4**, 953–963 (2022).
- <sup>84</sup> **3.** Zhussip, M., Soltanayev, S. & Chun, S. Y. Extending stein’s unbiased risk estimator to train deep  
<sup>85</sup> denoisers with correlated pairs of noisy images. *Adv. neural information processing systems* **32** (2019).

**Supplementary Table S1.** Comparison of PSNR (upper table) and Pearson correlation coefficient (bottom table) along the z axis of the whole volume.

	RAW	DIP	N2N	N2F	N2S	N2V	Ne2Ne	SUPPORT	SN2N	SelfMirror	
	N	Mean	SD	Mean	SD	Mean	SD	Mean	SD	Mean	SD
P1	200	10.9506	0.329692	16.86438	0.674965	9.774281	0.734877	19.76731	0.351072	19.79267	0.333882
P2	200	13.42975	0.328997	17.6801	0.507668	8.600921	0.429859	20.1176	0.345384	20.07213	0.34231
P4	200	15.53226	0.3347	18.14332	0.441793	8.546839	1.16418	20.37607	0.348057	20.27257	0.337762
P8	200	17.15763	0.340737	18.35665	0.406074	11.86203	0.430972	20.56458	0.352618	20.56707	0.348242
P16	200	18.27186	0.346823	18.48599	0.416252	9.369837	0.495033	20.69206	0.351438	20.57866	0.352811
P32	200	18.96115	0.352923	18.54925	0.402634	8.952609	0.421913	20.76713	0.355287	20.64993	0.346722
P64	200	21.15832	0.353373	19.5779	0.449453	11.04928	0.562691	22.60849	0.351796	22.06577	0.334395
P128	200	26.94544	0.349095	21.43815	0.604669	6.32506	0.445921	27.68983	0.367992	27.1814	0.385181
P1	200	0.295594	0.029067	0.393787	0.084345	0.294115	0.030043	0.848588	0.030417	0.816502	0.03296
P2	200	0.395326	0.035559	0.460873	0.081308	0.484439	0.026852	0.90191	0.018768	0.881226	0.020384
P4	200	0.507774	0.040733	0.50907	0.079117	0.371928	0.054626	0.935558	0.011327	0.900662	0.015988
P8	200	0.61674	0.041785	0.530623	0.076451	0.53469	0.031486	0.952343	0.008763	0.917959	0.013791
P16	200	0.704773	0.039744	0.540943	0.07663	0.74532	0.029144	0.960382	0.006829	0.923234	0.011458
P32	200	0.765025	0.036185	0.544957	0.07561	0.645419	0.036834	0.964321	0.006386	0.934117	0.011272
P64	200	0.8488	0.027611	0.550273	0.074021	0.736616	0.034684	0.967209	0.006669	0.949223	0.008929
P128	200	0.949158	0.010695	0.550833	0.072841	0.779424	0.013059	0.969127	0.005847	0.951626	0.009055

	RAW	DIP	N2N	N2F	N2S	N2V	Ne2Ne	SUPPORT	SN2N	SelfMirror	
	N	Mean	SD	Mean	SD	Mean	SD	Mean	SD	Mean	SD
P1	200	0.295594	0.029067	0.393787	0.084345	0.294115	0.030043	0.848588	0.030417	0.816502	0.03296
P2	200	0.395326	0.035559	0.460873	0.081308	0.484439	0.026852	0.90191	0.018768	0.881226	0.020384
P4	200	0.507774	0.040733	0.50907	0.079117	0.371928	0.054626	0.935558	0.011327	0.900662	0.015988
P8	200	0.61674	0.041785	0.530623	0.076451	0.53469	0.031486	0.952343	0.008763	0.917959	0.013791
P16	200	0.704773	0.039744	0.540943	0.07663	0.74532	0.029144	0.960382	0.006829	0.923234	0.011458
P32	200	0.765025	0.036185	0.544957	0.07561	0.645419	0.036834	0.964321	0.006386	0.934117	0.011272
P64	200	0.8488	0.027611	0.550273	0.074021	0.736616	0.034684	0.967209	0.006669	0.949223	0.008929
P128	200	0.949158	0.010695	0.550833	0.072841	0.779424	0.013059	0.969127	0.005847	0.951626	0.009055

**Supplementary Table S2.** Comparison of PSNR (upper table) and Pearson correlation coefficient (bottom table) along the y axis of the whole volume.

	RAW				DIP				N2N				N2F				N2S				N2V				Ne2Ne				SUPPORT				SN2N				SelfMirror					
N	Mean	SD	Mean	SD	Mean	SD	Mean	SD	Mean	SD	Mean	SD	Mean	SD	Mean	SD	Mean	SD	Mean	SD	Mean	SD	Mean	SD	Mean	SD	Mean	SD	Mean	SD	Mean	SD										
P1	500	10.32101	0.934145	16.24151	0.926417	9.150612	1.07177	19.14149	0.934444	19.17017	0.937207	19.14969	0.930377	18.93	0.941523	21.92783	0.978561	24.03175	1.021257	25.58116	1.512296																					
P2	500	12.79951	0.945007	17.0822	0.922609	8.35399	1.349715	19.4886	0.962122	19.44449	0.947736	19.36716	0.948433	19.11585	0.940751	21.50262	0.944375	19.83471	0.871137	22.69603	1.36992																					
P4	500	14.90108	0.965481	17.55503	0.920335	7.902102	0.995563	19.7451	0.983899	19.64672	0.936124	19.58679	0.962646	19.35004	0.965319	20.04626	0.907677	19.80832	0.928016	23.38591	1.071918																					
P8	500	16.52548	0.985549	17.77565	0.929232	11.34461	0.982292	19.9329	0.996024	19.9434	0.974489	19.70733	0.973428	19.5151	0.97441	19.32636	0.91193	19.87064	0.961064	20.35772	1.00316																					
P16	500	17.6391	1.008054	17.90578	0.930581	9.816559	2.15727	20.06004	1.002289	19.94813	0.997295	19.82641	0.978062	19.65555	0.978833	19.37846	0.916929	21.34802	0.879704	20.50582	1.001502																					
P32	500	18.3281	1.025725	17.97192	0.932977	8.573821	1.157633	20.13497	1.007344	20.02291	0.98049	19.89921	0.981132	19.71086	0.977534	19.37367	0.917767	21.30186	0.926503	20.51018	1.010107																					
P64	500	20.52523	1.028133	19.03468	0.993506	10.69294	1.190018	21.97731	0.997757	21.44184	0.897739	21.64553	0.963814	21.53524	0.944555	20.73046	0.940709	22.35812	0.865825	22.20173	0.998294																					
P128	500	26.31261	1.010759	21.02446	1.296226	6.075152	1.413635	27.07574	0.94168	26.58353	0.957497	26.04194	0.984942	27.1174	0.915533	23.85145	1.394786	24.73519	1.134557	27.13914	0.977538																					
	RAW				DIP				N2N				N2F				N2S				N2V				Ne2Ne				SUPPORT				SN2N				SelfMirror					
N	Mean	SD	Mean	SD	Mean	SD	Mean	SD	Mean	SD	Mean	SD	Mean	SD	Mean	SD	Mean	SD	Mean	SD	Mean	SD	Mean	SD	Mean	SD	Mean	SD	Mean	SD	Mean	SD	Mean	SD								
P1	500	0.284942	0.065292	0.358643	0.133556	0.279268	0.069798	0.831668	0.062325	0.790498	0.088551	0.810127	0.072301	18.93	0.941523	0.629773	0.133195	0.808339	0.07218	0.885394	0.032643																					
P2	500	0.38079	0.080953	0.423605	0.146647	0.448448	0.096546	0.891554	0.041284	0.866336	0.054759	0.856684	0.052576	19.11585	0.940751	0.679787	0.124605	0.854115	0.05695	0.892459	0.021074																					
P4	500	0.488596	0.094619	0.470112	0.152368	0.341676	0.115372	0.929097	0.026445	0.895193	0.044728	0.889192	0.040382	0.90396	0.035983	19.5151	0.97441	0.748278	0.106735	0.868292	0.052385	0.921985	0.019307																			
P8	500	0.593612	0.101065	0.492322	0.153608	0.494028	0.140987	0.947823	0.020844	0.909047	0.03952	0.97441	0.768447	0.103224	0.8624	0.048487	0.94952	0.019614																								
P16	500	0.679557	0.100351	0.502813	0.153839	0.71193	0.136763	0.956528	0.017396	0.924352	0.066908	0.913764	0.032979	19.65555	0.978833	0.772912	0.102446	0.84461	0.039032	0.953297	0.018588																					
P32	500	0.739248	0.095872	0.50714	0.153898	0.608087	0.133726	0.960723	0.016128	0.928904	0.026612	0.917836	0.031832	19.71086	0.977534	0.775976	0.102083	0.866204	0.045649	0.956005	0.018217																					
P64	500	0.825253	0.079753	0.51299	0.153746	0.692138	0.129365	0.963843	0.014967	0.944443	0.024674	0.924582	0.029429	21.53524	0.944355	0.777699	0.101934	0.877161	0.02883	0.956448	0.018395																					
P128	500	0.936894	0.037787	0.513167	0.154266	0.756335	0.072582	0.965991	0.013702	0.945092	0.047788	0.924563	0.029532	27.1174	0.915533	0.77907	0.101733	0.78068	0.074608	0.95893	0.017504																					

**Supplementary Table S3.** Comparison of PSNR (upper table) and Pearson correlation coefficient (bottom table) along the x-axis of the whole volume.

N	RAW		DIP		N2N		N2F		N2S		N2V		Ne2Ne		SUPPORT		SN2N		SelfMirror		
	Mean	SD	Mean	SD	Mean	SD	Mean	SD	Mean	SD	Mean	SD	Mean	SD	Mean	SD	Mean	SD	Mean	SD	
P1	500	10.25975	1.022834	16.18374	0.844436	9.201711	1.346186	19.08057706	0.983091	19.1151284	0.995716	19.0887066	0.967691	18.87007154	0.964777	21.88169358	0.990594	23.983887	0.94521	25.55297	1.253987
P2	500	12.73801	1.037878	17.0244	0.85314	8.384509	1.495865	19.42702486	1.024647	19.38316442	1.007887	19.30575246	0.994715	19.05591802	0.972808	21.4526372	0.963136	19.774389	0.953496	22.66408	1.183316
P4	500	14.83927	1.056308	17.49947	0.860399	7.849347	1.006135	19.68321902	1.054699	19.59489502	1.034531	19.52498316	1.015424	19.28918452	1.015916	19.98997858	0.962316	19.746045	0.987273	23.338	0.93223
P8	500	16.46357	1.082494	17.71867	0.864667	11.34635	1.210286	19.87083988	1.076389	19.8822567	1.043222	19.6452737	1.028688	19.45366216	1.026528	19.26826498	0.975161	19.808898	1.020428	20.29534	1.08365
P16	500	17.57707	1.106002	17.84939	0.867651	9.455165	2.025047	19.99796808	1.084983	19.89063036	1.074447	19.76425144	1.038442	19.59423278	1.023017	19.32039306	0.980958	21.286908	0.925144	20.44347	1.082296
P32	500	18.26601	1.126903	17.91607	0.867354	8.522731	1.216913	20.07287648	1.090719	19.9578174	1.047031	19.83704952	1.041651	19.64935176	1.034779	19.31564262	0.982684	21.241376	0.971709	20.44776	1.092517
P64	500	20.46312	1.130246	18.98571	0.8972	10.82853	1.460064	21.9152395	1.06724	21.38493292	0.95944	21.58320658	1.004038	21.4742258	0.978505	20.67693402	0.986787	22.302709	0.859008	22.13899	1.066935
P128	500	26.25054	1.111412	21.01816	1.269017	6.168304	1.644019	27.0142399	0.933059	26.5214432	0.902613	25.98159034	0.879409	27.0569339	0.926779	23.83390026	1.413597	24.714923	1.039062	27.07204	0.938681

N	RAW		DIP		N2N		N2F		N2S		N2V		Ne2Ne		SUPPORT		N2N		SelfMirror		
	Mean	SD	Mean	SD	Mean	SD	Mean	SD	Mean	SD	Mean	SD	Mean	SD	Mean	SD	Mean	SD	Mean	SD	
P1	500	0.281308	0.074978	0.349967	0.133185	0.276429	0.075413	0.825693	0.070759	0.781176	0.10045	19.08871	0.967691	0.770133	0.091658	0.619011	0.144328	0.797962	0.087633	0.881789	0.033895
P2	500	0.375759	0.094172	0.413488	0.147553	0.440607	0.107052	0.888086	0.044521	0.859791	0.06866	19.30575	0.994715	0.812754	0.078697	0.669599	0.133105	0.84859	0.062461	0.889012	0.022232
P4	500	0.481506	0.112235	0.459491	0.153216	0.333834	0.120966	0.926684	0.030225	0.889371	0.070735	19.52498	0.1015424	0.832963	0.075898	0.743111	0.105869	0.858546	0.072089	0.91955	0.019663
P8	500	0.584763	0.122355	0.481117	0.154077	0.48758	0.154455	0.946111	0.023899	0.905222	0.044207	19.64527	1.028688	0.877984	0.052202	0.766375	0.098671	0.857782	0.05233	0.947165	0.021394
P16	500	0.669373	0.124351	0.491944	0.15352	0.685813	0.14875	0.955187	0.020334	0.921796	0.050449	19.76425	1.038442	0.885829	0.050636	0.7711343	0.09787	0.838502	0.045475	0.951241	0.019813
P32	500	0.728239	0.121869	0.496256	0.153174	0.595873	0.152075	0.959615	0.01843	0.924256	0.040241	19.833705	1.041651	0.893764	0.046606	0.774476	0.097574	0.860833	0.053705	0.953942	0.019386
P64	500	0.813747	0.107145	0.502337	0.152024	0.69059	0.142262	0.962873	0.016524	0.940757	0.060481	21.58321	1.004038	0.912326	0.035929	0.776321	0.097294	0.873	0.034699	0.954497	0.01954
P128	500	0.928919	0.057951	0.502928	0.151989	0.748288	0.091673	0.965135	0.014574	0.943708	0.040476	25.98159	0.879409	0.967529	0.010575	0.777981	0.097212	0.77024	0.086257	0.956838	0.018941